

A statistical procedure for the identification of positrons in the PAMELA experiment

O. Adriani^{a,b}, G. C. Barbarino^{c,d}, G. A. Bazilevskaya^e, R. Bellotti^{f,g,*}, M. Boezio^h, E. A. Bogomolovⁱ, L. Bonechi^{a,b}, M. Bongi^b, V. Bonvicini^h, S. Borisov^{j,k,l}, S. Bottai^b, A. Bruno^{f,g}, F. Cafagna^g, D. Campana^d, R. Carbone^{j,d}, P. Carlson^m, M. Casolino^k, G. Castelliniⁿ, L. Consiglio^d, M. P. De Pascale^{j,k}, C. De Santis^k, N. De Simone^{j,k}, V. Di Felice^{j,k}, A. M. Galper^l, W. Gillard^m, L. Grishantseva^l, P. Hofverberg^m, G. Jerse^{h,o}, S. V. Koldashov^l, S. Y. Krutkovⁱ, A. N. Kvashnin^e, A. Leonov^l, V. Malvezzi^k, L. Marcelli^k, W. Menn^p, V. V. Mikhailov^l, E. Mocchiutti^h, A. Monaco^{f,g}, N. Mori^b, N. Nikonov^{j,k,i}, G. Osteria^d, P. Papini^b, M. Pearce^m, P. Picozza^{j,k}, M. Ricci^q, S. B. Ricciarini^b, L. Rossetto^m, M. Simon^p, R. Sparvoli^{j,k}, P. Spillantini^{a,b}, Y. I. Stozhkov^e, A. Vacchi^h, E. Vannuccini^b, G. Vasilyevⁱ, S. A. Voronov^l, J. Wu^m, Y. T. Yurkin^l, G. Zampa^h, N. Zampa^h, V. G. Zverev^l, D. Marinucci^r

^a *University of Florence, Department of Physics, Via Sansone 1, I-50019 Sesto Fiorentino, Florence, Italy.*

^b *INFN, Sezione di Florence, Via Sansone 1, I-50019 Sesto Fiorentino, Florence, Italy.*

^c *University of Naples "Federico II", Department of Physics, Via Cintia, I-80126 Naples, Italy.*

^d *INFN, Sezione di Naples, Via Cintia, I-80126 Naples, Italy.*

^e *Lebedev Physical Institute, Leninsky Prospekt 53, RU-119991 Moscow, Russia.*

^f *University of Bari, Department of Physics, Via Amendola 173, I-70126 Bari, Italy.*

^g *INFN, Sezione di Bari, Via Amendola 173, I-70126 Bari, Italy.*

^h *INFN, Sezione di Trieste, Padriciano 99, I-34012 Trieste, Italy.*

ⁱ *Ioffe Physical Technical Institute, Polytekhnicheskaya 26, RU-194021 St. Petersburg, Russia.*

^j *University of Rome "Tor Vergata", Department of Physics, Via della Ricerca Scientifica 1, I-00133 Rome, Italy.*

^k *INFN, Sezione di Roma "Tor Vergata", Via della Ricerca Scientifica 1, I-00133 Rome, Italy.*

^l *Moscow Engineering and Physics Institute, Kashirskoe Shosse 31, RU-11540 Moscow, Russia.*

^m *KTH, Department of Physics, and the Oskar Klein Centre for Cosmoparticle Physics, AlbaNova University Centre, 10691 Stockholm, Sweden.*

*Corresponding author. Tel: +390805443173

Email address: roberto.bellotti@ba.infn.it (R. Bellotti)

ⁿ*IFAC, Via Madonna del Piano 10, I-50019 Sesto Fiorentino, Florence, Italy.*

^o*University of Trieste, Department of Physics, Via A. Valerio 2, I-34147 Trieste, Italy .*

^p*University of Siegen, D-57068 Siegen, Germany.*

^q*INFN, Laboratori Nazionali di Frascati, Via Enrico Fermi 40, I-00044 Frascati, Italy.*

^r*University of Rome "Tor Vergata", Department of Mathematics, Via della Ricerca Scientifica 1, I-00133 Rome, Italy.*

Abstract

The PAMELA satellite experiment has measured the cosmic-ray positron fraction between 1.5 GeV and 100 GeV. The need to reliably discriminate between the positron signal and proton background has required the development of an ad hoc analysis procedure. In this paper, a method for positron identification is described and its stability and capability to yield a correct background estimate is shown. The analysis includes new experimental data, the application of three different fitting techniques for the background sample and an estimate of systematic uncertainties due to possible inaccuracies in the background selection. The new experimental results confirm both solar modulation effects on cosmic-rays with low rigidities and an anomalous positron abundance above 10 GeV.

Keywords:

Cosmic-rays, Positron, Classification, Wavelets, Electromagnetic calorimeter

1. Introduction

Recent measurements of cosmic-ray electrons and positrons carried out by the ATIC [1], PAMELA [2] FERMI [3] and HESS experiments [4], extend the previous balloon-borne [5, 6, 7, 8, 9, 10], and satellite [11] measurements and represent a breakthrough in cosmic-ray physics. In particular it is well known that an antimatter component that cannot be explained as an effect of a purely secondary production mechanism, could provide insight into the nature and distribution of particle sources in our galaxy [12]. The PAMELA experiment has reported a measurement of the positron fraction, *i.e.* the ratio of positron flux to the sum of electron and positron fluxes, $R = \phi(e^+)/(\phi(e^-) + \phi(e^+))$, at energies between 1.5 GeV and 100 GeV, sampled in 16 energy bins. The observations extend the energy range of previous positron measurements and unambiguously show an anomalous positron abundance above 10 GeV. A reliable identification of electrons and positrons has been performed by combining information from independent detectors within the apparatus [2, 13]. The main difficulty in the measurement of R is the dominating background flux from protons which is 10^3 (at 1 GV) and 10^4 (at 100 GV), times the positron flux. Furthermore, a precise estimate of the proton contamination in the positron sample is a difficult task.

A widely adopted approach both in high energy physics and astrophysics, consists of an intensive use of simulated signal and background samples to train different multivariate classifiers, such as artificial neural networks and support vector machines [15, 16]. It has been demonstrated that such an approach can improve background rejection in the signal sample [17, 18]. However this approach can introduce systematic uncertainties which are difficult to estimate, for the real data.

In this paper we present a method used to obtain an updated the PAMELA positron fraction [2] and further statistical procedures, based on wavelet and kernel estimates, in order to estimate the proton contamination in the positron sample. Although our approach is based on well known statistical techniques, we believe this methodology can be of interest because the data analysis is mainly based on the discrimination capabilities of a single detector, *i.e.* the electromagnetic calorimeter. Previously published results [2] refer to data collected by the experiment between July 2006 and February 2008. Here, we present the methodology applied to larger data set collected between July 2006 and December 2008.

In Section 2 the PAMELA experiment is briefly described. A detailed

description of the apparatus can be found in [19]. In Section 3 the discriminating variables used for the analysis are presented. In Section 4 the event selection procedure is described: this is the first phase of the analysis and it involves all the detectors of the PAMELA apparatus. The core of the analysis is described in Section 5. The methodologies developed to estimate the positron fraction R and the statistical and systematic uncertainties are illustrated and applied to the PAMELA data. A summary of the experimental results and the conclusions are presented in Section 6.

2. The PAMELA apparatus

As shown in Fig 1, the PAMELA apparatus is composed by the following detectors (from top to bottom):

1. a time-of-flight system (ToF (S1, S2, S3));
2. a magnetic spectrometer;
3. an anticoincidence system (AC (CARD, CAT, CAS));
4. an electromagnetic imaging calorimeter;
5. a shower tail catcher scintillator (S4) and
6. a neutron detector.

The ToF system provides a fast signal for triggering the data acquisition and measures the time-of-flight and ionization energy losses (dE/dx) of traversing particles. It also allows down-going particles to be reliably identified. Multiple tracks, produced in interactions above the spectrometer, are rejected by requiring that only one strip of the top ToF scintillator (S1 and S2) layers register an energy deposition (hit). Similarly no hits were permitted in either top scintillators of the AC system (CARD and CAT). The magnetic spectrometer consists of a 0.43 T permanent magnet and a silicon microstrip tracking system. It measures the rigidity of charged particles through their deflection in the magnetic field. During flight the spatial resolution is observed to be $3 \mu\text{m}$ in the bending view, corresponding to a Maximum Detectable Rigidity (MDR), defined as a 100% uncertainty in the

rigidity determination, exceeding 1 TV. The dE/dx losses measured in S1 and the silicon layers of the magnetic spectrometer were used to select minimum ionizing singly charged particles (mip) by requiring the measured dE/dx to be less than twice that expected from a mip. The sampling calorimeter comprises 44 silicon sensor planes interleaved with 22 plates of tungsten absorber. Each tungsten layer has a thickness of 0.26 cm corresponding to 0.74 radiation lengths. A high dynamic-range scintillator system (S4) and a neutron detector are mounted under the calorimeter. The apparatus is approximately 130 cm tall and with a mass of about 470 kg and it is inserted inside a pressurized container attached to the Russian Resurs-DK1 satellite [19].

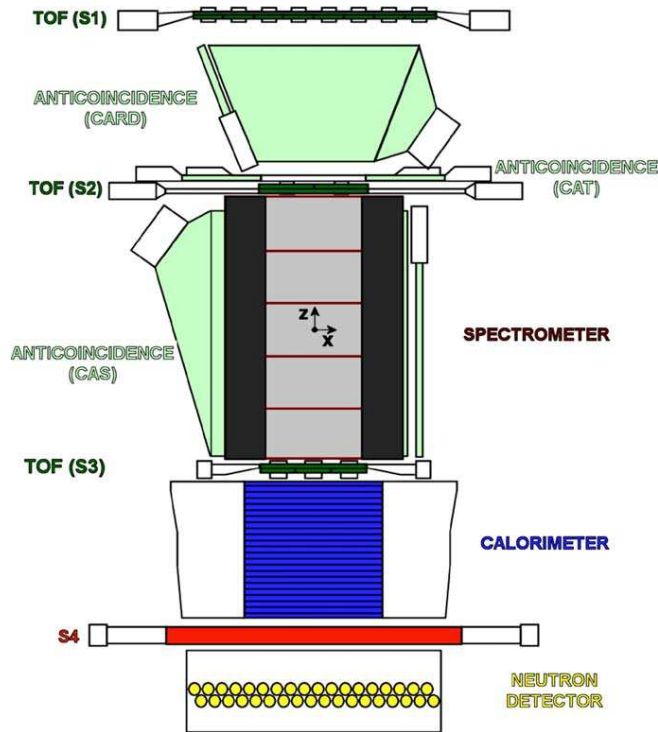


Figure 1: A schematic overview of the PAMELA satellite experiment. The experiment stands ~ 1.3 m high and, from top to bottom, consists of a time-of-flight (ToF) system (S1, S2, S3 scintillator planes), an anticoincidence shield system, a permanent magnet spectrometer (the magnetic field runs in the y -direction), a silicon-tungsten electromagnetic calorimeter, a shower tail scintillator (S4) and a neutron detector. The experiment has an overall mass of 470 kg.

2.1. The imaging calorimeter

In this analysis the PAMELA silicon-tungsten sampling imaging calorimeter [20] plays a key role, due to its capability to give an accurate topological description of the showers generated by the interaction of the cosmic-ray particles.

Electromagnetic calorimeters have been widely used for particle discrimination in balloon-borne cosmic-ray experiments [5, 7, 21, 22]. The PAMELA an imaging calorimeter is evolution of the instrument used in several balloon-borne experiments [22, 23, 6] and its performances have been thoroughly investigated by means of test beam data and Monte Carlo simulations [20]. It is 16.3 radiation lengths (0.6 nuclear interaction lengths) deep, so both electrons and positrons develop a well-contained electromagnetic shower in the energy range of interest. In contrast, the majority of the protons will either pass through the calorimeter as a minimum ionizing particle or interact deeply in the calorimeter. In fact there is a high probability (>89%) that an electromagnetic shower will start in the first 3 planes of the calorimeter. For hadronic showers, the starting point is distributed more uniformly. Particle identification based on the total measured energy and the starting point of the reconstructed shower in the calorimeter can be tuned to reject 99.9% of the protons, while selecting more than 95% of the electrons or positrons. The remaining proton contamination in the positron sample can be eliminated using additional topological information, including the lateral and longitudinal profile of the shower. Using particle beam data collected at CERN it was previously shown that less than one proton out of 100,000 passes the calorimeter electron selection up to 200 GeV/c, with a corresponding electron selection efficiency of 80% [20].

3. Discriminating variable selection

The misidentification of electrons and protons are the largest sources of background when estimating the positron fraction. This can occur if the sign-of-charge is incorrectly assigned from the spectrometer data, or if electron- and proton-like interaction patterns are confused in the calorimeter data. The proton-to-positron flux ratio increases from approximately 10^3 at 1 GeV to approximately 10^4 at 100 GeV and represents the major source of contamination. Robust positron identification is therefore required and the residual proton background must be carefully assessed. To do this a single discriminating variable is considered: the fraction \mathcal{F} of calorimeter energy deposited

inside a cylinder of radius 0.3 Molière radii. Fig. 2 shows \mathcal{F} as a function of deflection (rigidity⁻¹). The axis of the cylinder is defined by extrapolating the particle track reconstructed in the spectrometer. The Molière radius is an important quantity in calorimetry as it quantifies the lateral spread of an electromagnetic shower (about 90% of the shower energy is contained in a cylinder with a radius equal to 1 Molière radius), and depends only on the absorbing material (tungsten in this case). The events shown in Fig. 2 were selected requiring a match between the momentum measured by the tracking system and the total detected energy and the starting point of the shower in the calorimeter. For negatively-signed deflections, electrons are clearly visible as a horizontal band with \mathcal{F} lying mostly between 0.4 and 0.7. For positively-signed deflections, the similar horizontal band is naturally associated to positrons, with the remaining points, mostly at $\mathcal{F} < 0.4$, designated as proton contamination. The validity of such event characterization was confirmed using the neutron yield from the calorimeter and the ionization (dE/dx) losses measured in the spectrometer [13]. The spillover limit for positrons is estimated from particle beam tests to be approximately 300 GeV. From particle beam tests the spillover limit for protons is estimated to be approximately 300 GeV, primarily due to the tracker resolution. The electron spillover background between 1.5 and 100 GeV is negligible.

4. Event selection

While the distribution shown in Fig. 2 presents a clear positron signature, the residual proton background distribution must be quantified. It is worthwhile to note that the background distribution was obtained using the flight calorimeter data and there was no dependence on simulations. In order to build a background model, the total calorimeter depth of 22 detector planes was divided in two non-mutually exclusive parts: an upper part comprising planes 1 – 20, and a lower part comprising planes 3 – 22. The positron component in positively charged events can be significantly reduced by selecting particles that do not interact in the first 2 planes because only 2% of electrons and positrons with rigidities greater than 1.5 GV pass this condition. This requirement selects a nearly pure sample of protons entering the lower part of the calorimeter (planes 3 – 22). The event selection methodology was further validated using particle beam data collected prior to launch and data generated using the PAMELA Collaboration’s official simulation program. This simulation is based on the GEANT package [24] version 3.21 and

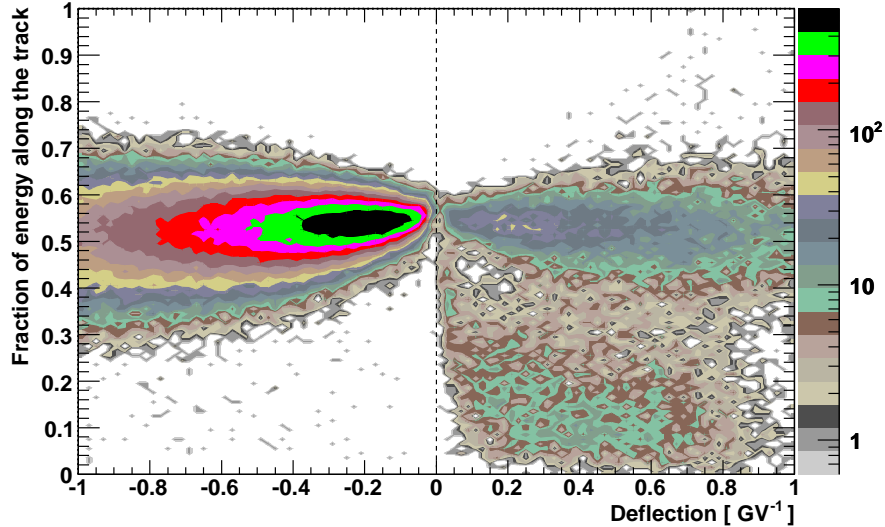


Figure 2: Calorimeter energy fraction \mathcal{F} . The fraction of calorimeter energy deposited inside a cylinder of radius 0.3 Molière radii, as a function of deflection. The number of events per bin is shown in different colours, as indicated in the colour scale. The axis of the cylinder is defined by extrapolating the particle track reconstructed by the spectrometer. The events were selected requiring a match between the momentum measured by the tracking system and the total detected energy and requiring that the electromagnetic shower starts developing in the first planes of the calorimeter.

reproduces the entire PAMELA apparatus.

Calorimeter variables (e.g. total detected energy, and lateral shower spread) were evaluated for the upper and lower parts of the calorimeter. Electrons and positrons were identified in the upper part of the calorimeter using the total detected energy and the starting point of the shower. As an example Fig. 3 shows the energy fraction \mathcal{F} , for negatively charged particles in the rigidity range 28 – 42 GV selected as electrons in the upper half of the calorimeter (panel a). Panels (b) and (c) show the \mathcal{F} distributions for positively-charged particles obtained for the lower (upper) part of the calorimeter, i.e. protons (protons and positrons). The distributions in panels (a) and (b) are clearly different while panel (c) shows a mixture of the two distributions, which strongly supports the positron interpretation for the electron-like \mathcal{F} distribution in the sample of positively charged events.

5. Positron/proton discrimination

As a result of the event selection described in the last section we obtained the distributions of pure electrons, pure protons and a mixture of positrons and protons, as shown in Fig. 3. Starting from these distributions the deter-

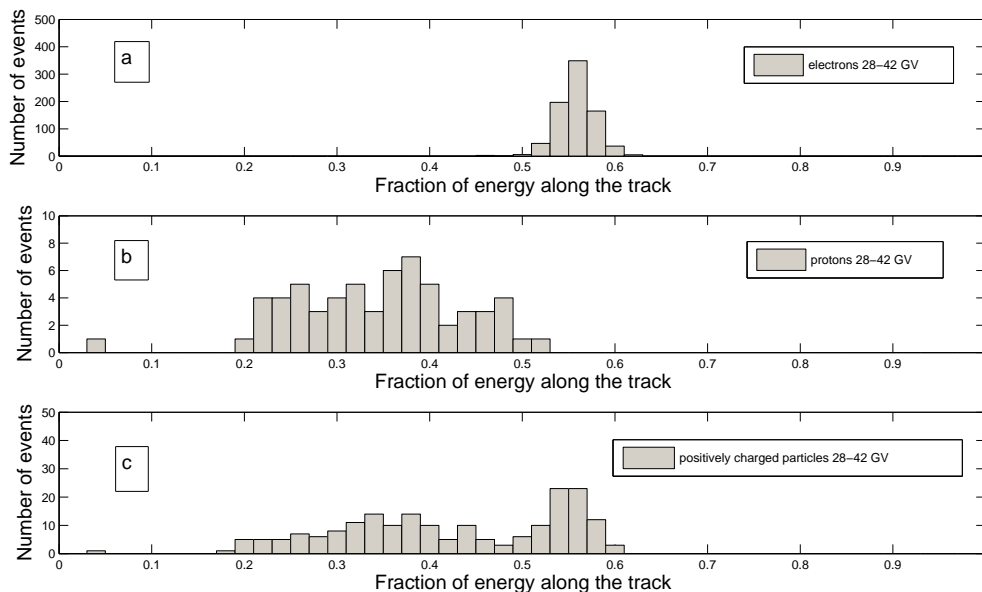


Figure 3: Calorimeter energy fraction \mathcal{F} : 28 – 42 GeV. Panel (a) shows the distribution of the energy fraction for negatively charged particles, selected as electrons in the upper part of the calorimeter. Panel (b) shows the same distribution for positively charged particles selected as protons in the bottom part of the calorimeter. Panel (c) shows positively charged particles, selected in the upper part of the calorimeter, i.e. protons and positrons.

mination of the ratio R , with the statistical and systematic error estimates, consists of four main steps, as summarised in Fig. 4:

1. estimation of the probability density functions (pdf) for the experimental distributions shown in Fig. 3;
2. construction of a finite mixture density of probability;

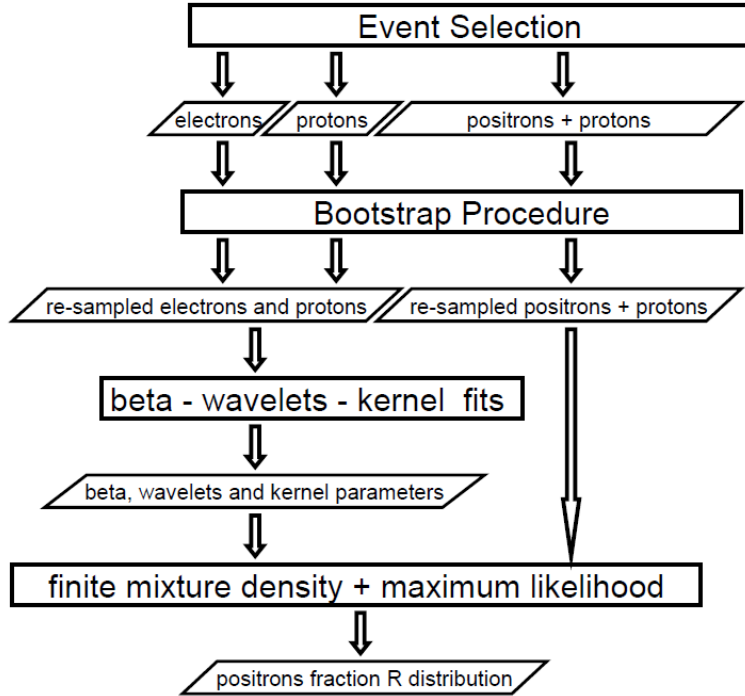


Figure 4: Flowchart of the methodology, based on different fitting and bootstrap techniques developed to evaluate the positron fraction R .

3. estimation of the weight of the mixture by means of the maximum likelihood indicator;
4. estimation of the statistical errors by means of a bootstrap procedure.

In addition, an estimate of the systematic uncertainties due to inaccuracies in the background identification is performed.

5.1. Pdf estimate

The proton experimental distributions provide information about the background yields. In order to evaluate these distributions and to check possible systematic errors in this phase of the analysis, three different methods have been implemented: beta, wavelets and kernel.

5.1.1. Beta pdf

Since the discriminating variable used for the analysis is the energy fraction \mathcal{F} , spanning the interval $[0, 1]$, the rational choice is to fit the experimental distribution with a function spanning in the same interval and with few free parameters, in order to avoid unphysical modeling of the experimental data. We used the beta function [28]:

$$f(x) = \frac{1}{\beta(p, q)} x^{p-1} (1-x)^{q-1}. \quad (1)$$

where $p > 0$, $q > 0$, and $\beta(p, q)$ is

$$\beta(p, q) = \int_0^1 x^{p-1} (1-x)^{q-1} dx. \quad (2)$$

This density has been used to fit both electrons and protons. A set of parameters for each rigidity bins is obtained and used for the subsequent steps of the analysis.

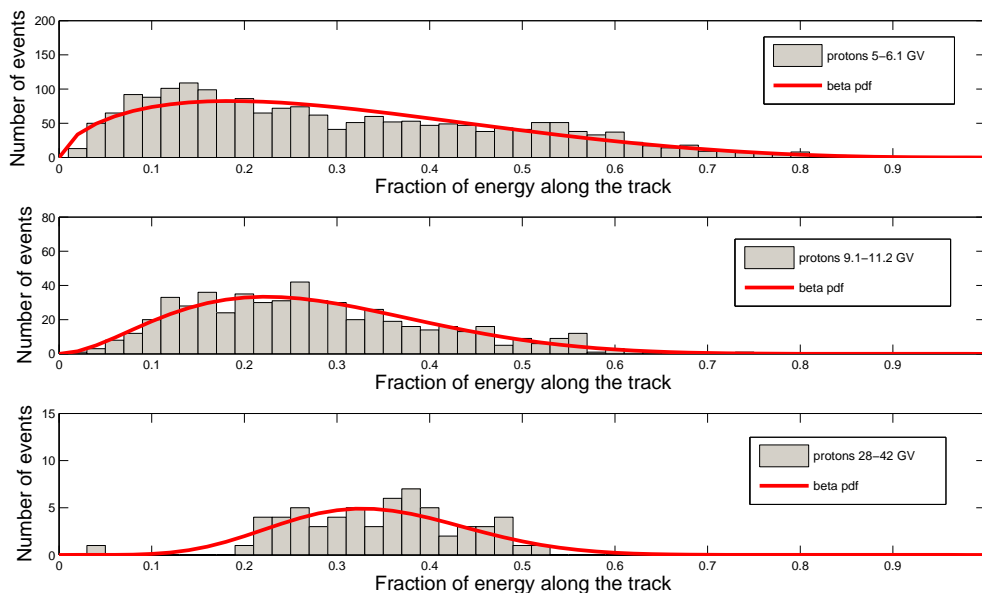


Figure 5: Distribution of the energy fraction for positively charged particles selected as protons for 3 different rigidity bins with a fit to a beta pdf.

The mean of the beta pdf is:

$$\bar{x} = \frac{p}{p+q} \quad (3)$$

and its variance is:

$$\sigma^2 = \frac{pq}{(p+q)^2 + (p+q+1)}. \quad (4)$$

5.1.2. Wavelets

In the previous section, the distribution of the energy fraction was fitted by means of a fixed family, i.e. we fitted a *parametric* law in the statistical jargon. More precisely, we assumed a priori that the experimental distributions we observed should be generated according to a specific (beta) law in $[0, 1]$. Although the choice of a beta function is natural for random variables in this range, it is important to question how much our final results depend on this assumption, i.e. their degree of robustness when varying the energy fraction distribution over a much greater range of possibilities. Our goal here is to explore the possibility of a *nonparametric* fit, where there is no a priori assumption on the energy fraction distribution.

Over the last fifteen years, the statistical literature has focussed on the estimation of density functions in this broader nonparametric setting. We refer for instance to [31] for an introduction to this area of research. A wide consensus has formed on the role of wavelet based methods as the most powerful statistical techniques for nonparametric density estimation.

A wavelet system is essentially an orthonormal basis which is constructed by dilations and translations of a mother and father function, leading to a multiresolution scheme. The wavelets we are going to implement are those proposed by Daubechies, which are computationally convenient as their support in the real domain is limited. More explicitly, the *father wavelet* satisfies [31]:

$$\varphi(x) = \sqrt{2} \sum_k h_k \varphi(2x - k) \quad (5)$$

where h_k are suitably chosen weights ([33]), whereas the *mother wavelet* satisfies:

$$\psi(x) = \sqrt{2} \sum_k (-1)^{k+1} h_{1-k} \varphi(2x - k) \quad (6)$$

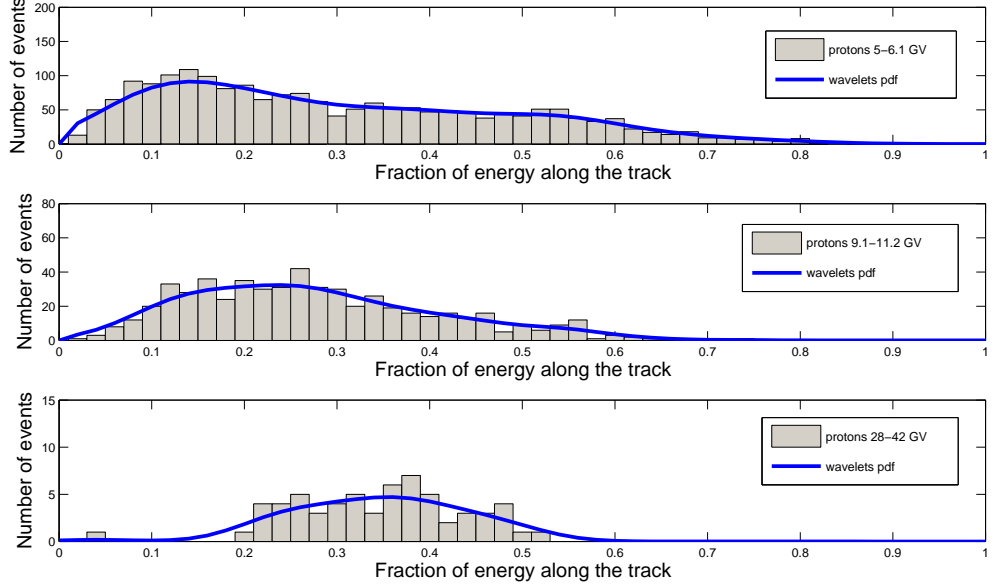


Figure 6: Distribution of the energy fraction for positively charged particles selected as protons for 3 different rigidity bins with a wavelets fit.

The multiresolution expansion of a function f is then provided by:

$$f(x) = \sum_k \alpha_k \varphi_k(x) + \sum_{j,k} \beta_{jk} \psi_{jk}(x) \quad (7)$$

where α_k and β_{jk} are approximation and detail coefficients, respectively, and the elements of the basis are constructed as

$$\psi_{jk}(x) = 2^{j/2} \psi(2^j x - k), \quad j, k = 1, 2, \dots \quad (8)$$

In practice the coefficients α_k and β_{jk} are unknown and must be estimated from the data. Given x_1, \dots, x_n independent identically distributed random variables with an unknown density f on \mathbb{R} , suitable estimators are provided by

$$\hat{\alpha}_k = \frac{1}{n} \sum_{i=1}^n \varphi_k(x_i), \quad \hat{\beta}_{jk} = \frac{1}{n} \sum_{i=1}^n \psi_{jk}(x_i). \quad (9)$$

These estimators can be viewed as convolutions of the empirical histograms of the observations with the elements of the wavelets basis. At this stage, an obvious estimator may be proposed, by simply replacing the coefficients α , β in (7) by their sample estimates. This approach - the so called *linear wavelet estimator* - has however been shown to be suboptimal in general ([31] or [32]). On the other hand, a wide consensus has emerged in the mathematical statistics community on the use of so-called wavelet thresholding techniques. Here, *small* coefficients are suppressed by introducing a threshold. In particular, in this paper a *hard thresholding rule* is used. In this case, the estimator for f is defined by [31]:

$$\hat{f}_n(x) = \sum_k \hat{\alpha}_k \varphi_k(x) + \sum_{j,k} \hat{\beta}_{jk}^H \psi_{jk}(x) \quad (10)$$

where the coefficients $\hat{\beta}_{jk}^H$ are defined by:

$$\hat{\beta}_{jk}^H = \hat{\beta}_{jk} I(|\hat{\beta}_{jk}| > t) \quad (11)$$

(the indicator function is defined as usual, e.g. $I(|X| > t) = 1$ if $|X| > t$, 0 otherwise). The threshold level is chosen to be

$$t = c \sqrt{\frac{\log n}{n}} \quad (12)$$

where $c > 0$ is a suitably chosen constant, and n is the number of observations in our sample. Intuitively, the rationale behind these techniques can be explained as follows. The smaller sample coefficients can be expected to be largely dominated by noise, so dropping them will improve the global performance of the estimates. These argument can be made rigorous, in particular it can be shown that wavelet thresholding estimators yield basically the optimal rate of convergence over a wide variety of loss functions, i.e., they (nearly) minimize over a wide class of functions f and norms $\|\cdot\|_{L^p}$ the maximum risk

$$\mathbb{R}(\hat{f}_n, f) = \max_f \langle \|\hat{f}_n - f\|_{L^p}^p \rangle \quad (13)$$

In practice, this means wavelet thresholding techniques enjoy robustness properties which are important in our context. They are sensitive at the same time to large scale features of the unknown energy distribution, and

they are also expected to detect the possible existence of small scale effects, such as local density spikes which could affect the final result. We refer again to [31] and [32] for further details and discussion.

To fit the proton sample, the wavelet thresholding technique with the Daubechies' basis (in particular db3) has been used. A critical step has been to find the best value for the parameter c in (12). We started fixing $c = 3$, which is often recommended as rule-of-the-thumb choice. We further verified by numerical experiments that our results are very stable for a wide range of fluctuations around this value. The positron-to-electron ratio estimates and corresponding confidence intervals are very close (indeed, in some cases nearly undistinguishable) from those obtained with the parametric fit of the beta distribution.

5.1.3. Kernel estimate

The kernel estimate is a statistical technique used to obtain an unbinned and nonparametric estimate of the probability density function. In the univariate case, the general kernel estimate of the parent distribution is given by [36]:

$$f(x) = \frac{1}{nh} \sum_{i=1}^n K\left(\frac{x - x_i}{h}\right) \quad (14)$$

where x_i represents the data and h is the smoothing parameter (also called the bandwidth). It is important to note that $f(x)$ is bin-independent regardless of choice of K . K has the role to distribute the contribution of each data point in the evaluation of the probability density function. Instead h have the task to set the scale of kernel.

Since the discriminating variable is defined in the bounded interval $[0, 1]$ a beta kernel has been used [38]. The beta kernel is a non-negative kernel and it is usually considered to estimate probability density functions with compact supports.

The number of beta functions generated was equal to the number of bins of the histogram and each beta function had a mean equal to the center of histogram bins. The standard deviation of these functions has been chosen through an application of the Kolmogorov-Smirnov test so that the initial distribution of protons and the modified one were statistically compatible, thereby rejecting the null hypothesis at 5% level.

The beta parameters (p, q) have been calculated inverting (3) and (4). The kernel bandwidth is assumed to be the histogram bin. The number of

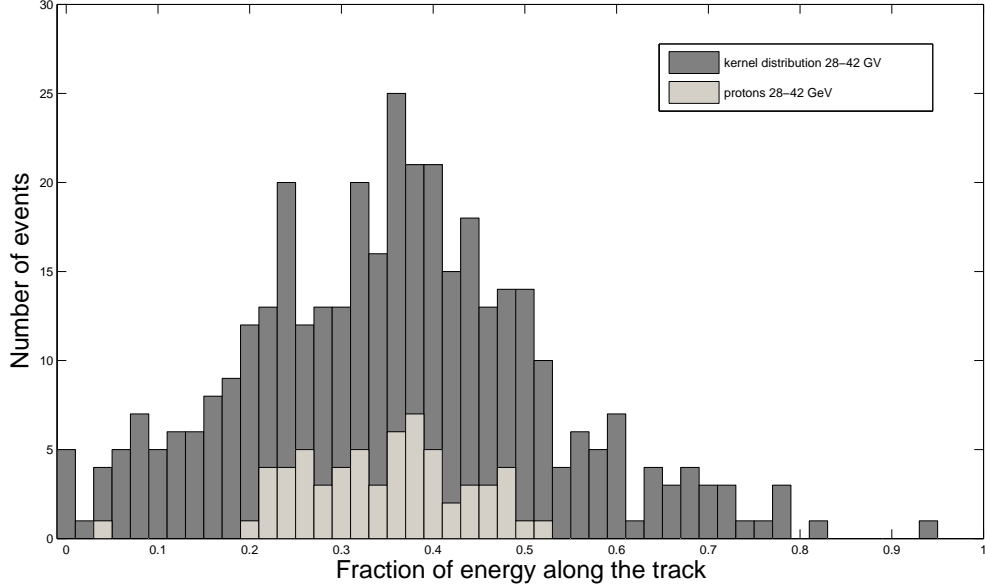


Figure 7: The distribution of positively charged particles selected as protons (grey) for the rigidity bin 28 – 42 GV and the same distribution modified using the kernel method (dark-grey).

events in each histogram of protons has been increased six fold compared to the original histogram. Fig. 7 shows the real protons and the pseudo-proton set for rigidity between 28 GV and 42 GV. Each pseudo-proton sample is then analyzed in the same way as the real protons (in particular with wavelets-fit), obtaining, for each energy bin, a new positron fraction.

5.2. Finite mixture density

A finite mixture of distributions is used for modelling dataset extracted from not homogeneous population. It is useful to analyze a sample drawn from an unknown mixture of known distributions. In the procedure of the finite mixture distributions an experimental distribution may be approximated as a linear combination of probability distribution functions (pdfs) [26]:

$$g(x, p) = \sum_{i=1}^n p_i f_i(x) \quad (15)$$

where $g(x, p)$ is the pdf to estimate, $f_i(x)$ are known pdfs, n is the number of pdfs, p_i are the mixing proportions ($0 < p_i < 1$ and $\sum_{i=1}^n p_i = 1$) to estimate.

In the present analysis we model, for each energy interval, the distribution of the calorimeter energy fraction (\mathcal{F}) for positively-charged particles as mixture distribution [26] of the positrons and protons pdfs:

$$g(\mathcal{F}) = pf_b(\mathcal{F}) + (1 - p)f_s(\mathcal{F}) \quad (16)$$

where $f_b(\mathcal{F})$ and $f_s(\mathcal{F})$ are the probability density functions for protons and electrons, respectively and the pdfs f_b and f_s have been determined in the previous section. As a result of this phase of the analysis a set of unknown weights p_j , with $j = 1, \dots, 16$, is obtained.

5.3. Maximum Likelihood

In order to find the values of unknown weights p_j we used the well known maximum likelihood method. In the present case the likelihood function, (for each rigidity bin), is

$$L_j = \prod_{t=1}^m \left[p_j f_b(\mathcal{F}_t) + (1 - p_j) f_s(\mathcal{F}_t) \right]. \quad (17)$$

where m is the number of independent observations x_1, x_2, \dots, x_m in each rigidity bin.

The estimation of the parameters p_j is done by maximizing the natural logarithm of (17):

$$\frac{\partial \ln L_j}{\partial p_j} = 0. \quad (18)$$

As a result of the three steps of the analysis, three different weights of the mixture for each energy bin are obtained. Using the beta functions, the wavelets transform and the kernel technique. In the next section the bootstrap technique is introduced. It has been used to evaluate both the positron fraction R and the statistical errors of the measurements.

5.4. Statistical error estimates by means of the bootstrap technique

The Bootstrap is a powerful method for analyzing small expensive-to-collect data sets where prior information is sparse [34]. In this method, a set of data is randomly resampled many times with replacement. Then

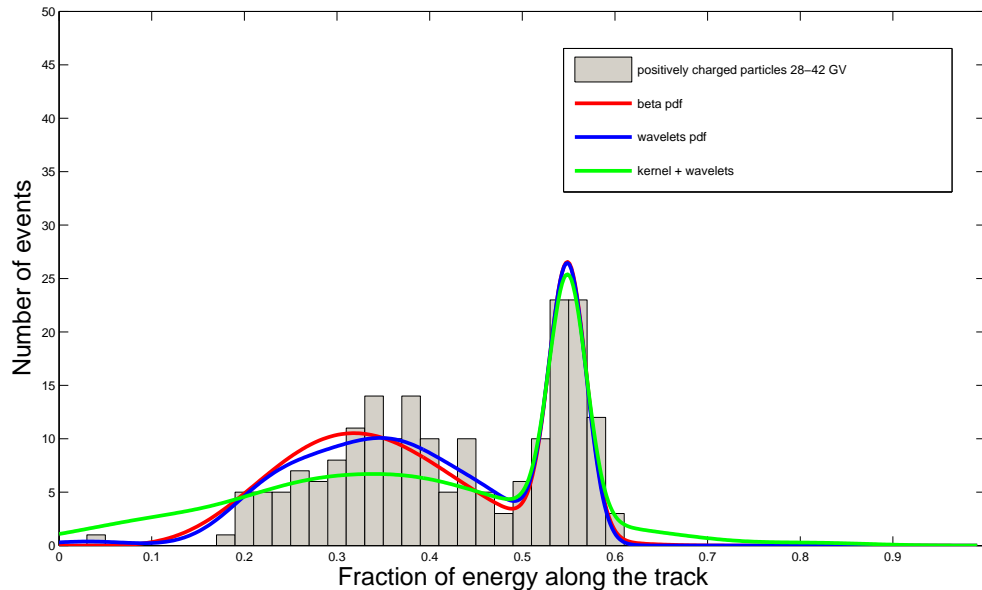


Figure 8: The distribution of positively charged particles for the rigidity bin 28-42 GV showing 3 pdf fits.

statistical indicators, such as the standard error or the confidence interval, are evaluated from these new samples [35].

This procedure has been used to estimate the statistical error on the ratio R .

Each experimental distributions for electrons, protons and positively-charged particles have been resampled 1000 times, then the three steps of the analysis procedure previously described have been repeated. For each rigidity bin, a statistical distribution of the ratio R is thereby obtained.

As a first step, $M = 1000$ bootstrap resampling of positives sample were applied. For each re-sample i the unknown parameter p_i was estimated by means of an un binned maximum likelihood analysis. As a second step the procedure has been repeated $N = 1000$ times applying N bootstrap resampling of electron and proton sample. So $N \times M$ estimations of the number of positron candidates have been obtained. Then, the final number

Rigidity at spectrometer (GV)	Percent error (beta)	Percent error (wavelets)	Percent error (kernel with wavelets)
1.5 – 1.8	3.2%	2.6%	2.6%
1.8 – 2.2	2.6%	2.9%	2.6%
2.2 – 2.7	2.7%	2.6%	2.6%
2.7 – 3.3	2.9%	3.1%	3.1%
3.3 – 4.1	3.1%	3.9%	3.9%
4.1 – 5.0	3.6%	3.8%	4.3%
5.0 – 6.1	3.9%	5.7%	5.3%
6.1 – 7.4	4.7%	4.8%	4.4%
7.4 – 9.1	4.9%	4.9%	5.0%
9.1 – 11.2	4.7%	5.7%	5.9%
11.2 – 15.0	5.3%	5.0%	5.6%
15.0 – 20.0	6.1%	5.4%	6.3%
20.0 – 28.0	8.1%	7.5%	8.2%
28.0 – 42.0	10.1%	9.5%	11.2%
42.0 – 65.0	13.4%	12.4%	13.0%
65.0 – 100.0	25%	29.5%	25.3%

Table 1: Statistical errors on the positron fraction R for all rigidity bins.

of positron candidates was obtained as:

$$\bar{n} = \frac{1}{N} \sum_{i=1}^N \left(\frac{1}{M} \sum_{j=1}^M n_{ji} \right) \quad (19)$$

where n_{ji} is the number of positron candidates evaluated by each bootstrap iteration. Therefore also $N \times M$ estimations of positron fraction have been obtained. In the present analysis we used the range from the 16th and 84th percentiles of these distributions as the statistical error estimates of the ratio R . As shown in Table 1 the statistical errors on the points range between 3% and 10% in all bins but the last two and then increase to just under 30% in the highest energy bin. Fig. 9 shows three new estimates of the positron fraction, using the different fitting techniques adopted in this study. Moreover, as shown in Tab. 2, the results obtained with the three different background pdfs are consistent with each other.

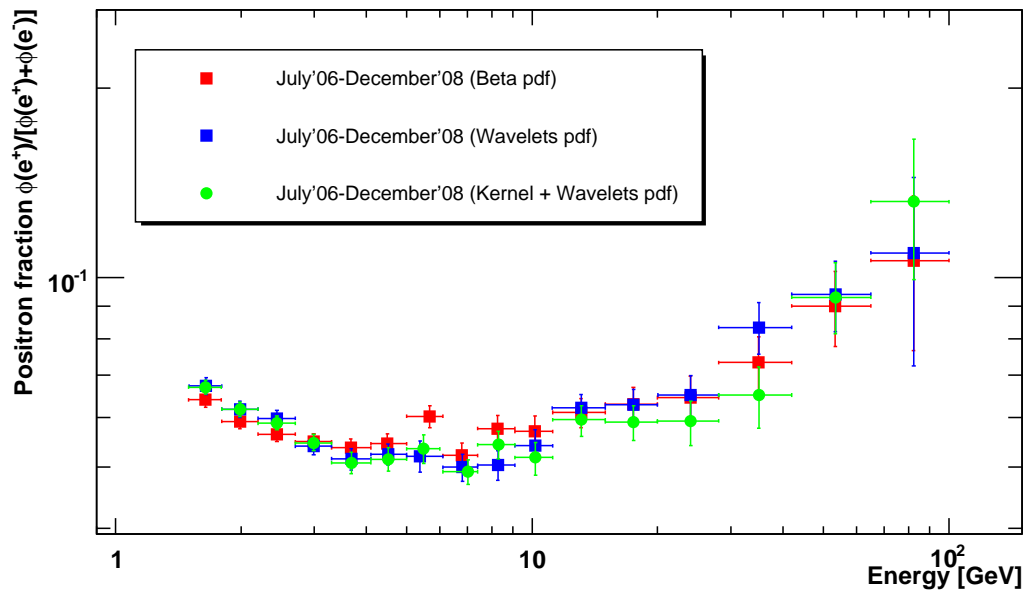


Figure 9: The positron fraction R obtained using the wavelets-fit (blue), beta-fit (red) and kernel with wavelets-fit (green).

5.5. Systematic uncertainties due to inaccuracies in the background selection

The main sources of systematic uncertainties in the determination of the positron fraction are investigated in the following. Due to the equivalence of the results obtained in the previous section with the three different pdfs, the evaluation of the systematic uncertainties has been performed using only the beta fit.

This is done by introducing a modification in the background distribution using the weighted bootstrap technique. This particular technique consists of positive weights applied to each observation of the dataset [39]. For each rigidity bin, starting from a proton sample $n(\mathcal{F})$ with mean \bar{x} , two new samples, $n^+(\mathcal{F})$ and $n^-(\mathcal{F})$, are generated:

1. $n^+(\mathcal{F})$ with mean $\bar{x}^+ > \bar{x}$;
2. $n^-(\mathcal{F})$ with mean $\bar{x}^- < \bar{x}$.

The bootstrap weights are chosen in order to have both $n^+(\mathcal{F})$ and $n^-(\mathcal{F})$ statistically incompatible with $n(\mathcal{F})$, according to the Kolmogorov-Smirnov test.

Rigidity at spectrometer (GV)	Mean kinetic energy at top of payload beta/wavelets/kernel (GeV)	Extrapolated $\frac{\phi(e^+)}{\phi(e^-)+\phi(e^+)}$ at top of payload with beta-fit	Extrapolated $\frac{\phi(e^+)}{\phi(e^-)+\phi(e^+)}$ at top of payload with wavelets-fit	Extrapolated $\frac{\phi(e^+)}{\phi(e^-)+\phi(e^+)}$ at top of payload with kernel with wavelets-fit
1.5 – 1.8	1.65 / 1.65 / 1.65	0.0639 ^{+0.0017} _{-0.0017}	0.0673 ^{+0.0021} _{-0.0021}	0.0670 ^{+0.0017} _{-0.0017}
1.8 – 2.2	1.99 / 1.99 / 1.99	0.0591 ^{+0.0015} _{-0.0015}	0.0618 ^{+0.0018} _{-0.0018}	0.0618 ^{+0.0016} _{-0.0016}
2.2 – 2.7	2.44 / 2.44 / 2.44	0.0564 ^{+0.0015} _{-0.0015}	0.0598 ^{+0.0017} _{-0.0014}	0.0587 ^{+0.0016} _{-0.0014}
2.7 – 3.3	2.99 / 2.99 / 2.99	0.0549 ^{+0.0016} _{-0.0016}	0.0540 ^{+0.0016} _{-0.0017}	0.0546 ^{+0.0018} _{-0.0015}
3.3 – 4.1	3.67 / 3.68 / 3.68	0.0537 ^{+0.0017} _{-0.0017}	0.0516 ^{+0.0019} _{-0.0021}	0.0508 ^{+0.0020} _{-0.0020}
4.1 – 5.0	4.49 / 4.51 / 4.52	0.0545 ^{+0.0020} _{-0.0020}	0.0524 ^{+0.0020} _{-0.0020}	0.0515 ^{+0.0022} _{-0.0022}
5.0 – 6.1	5.68 / 5.38 / 5.49	0.0602 ^{+0.0024} _{-0.0024}	0.0520 ^{+0.0030} _{-0.0029}	0.0535 ^{+0.0028} _{-0.0028}
6.1 – 7.4	6.78 / 6.80 / 7.02	0.0522 ^{+0.0024} _{-0.0024}	0.0500 ^{+0.0024} _{-0.0025}	0.0492 ^{+0.0022} _{-0.0022}
7.4 – 9.1	8.27 / 8.28 / 8.30	0.0576 ^{+0.0028} _{-0.0028}	0.0504 ^{+0.0027} _{-0.0027}	0.0543 ^{+0.0027} _{-0.0027}
9.1 – 11.2	10.16 / 10.17 / 10.18	0.0570 ^{+0.0033} _{-0.0033}	0.0541 ^{+0.0032} _{-0.0031}	0.0518 ^{+0.0029} _{-0.0032}
11.2 – 15.0	13.11 / 13.12 / 13.13	0.0611 ^{+0.0032} _{-0.0033}	0.0619 ^{+0.0032} _{-0.0030}	0.0595 ^{+0.0031} _{-0.0035}
15.0 – 20.0	17.50 / 17.51 / 17.51	0.0630 ^{+0.0039} _{-0.0039}	0.0628 ^{+0.0036} _{-0.0033}	0.0590 ^{+0.0039} _{-0.0036}
20.0 – 28.0	23.99 / 24.00 / 24.01	0.0645 ^{+0.0052} _{-0.0052}	0.0651 ^{+0.0048} _{-0.0051}	0.0592 ^{+0.0045} _{-0.0051}
28.0 – 42.0	34.97 / 35.00 / 34.99	0.0733 ^{+0.0073} _{-0.0074}	0.0833 ^{+0.0079} _{-0.0077}	0.0651 ^{+0.0071} _{-0.0074}
42.0 – 65.0	53.43 / 53.44 / 53.48	0.090 ^{+0.012} _{-0.013}	0.094 ^{+0.012} _{-0.012}	0.093 ^{+0.013} _{-0.012}
65.0 – 100.0	82.39 / 82.41 / 82.47	0.106 ^{+0.028} _{-0.030}	0.109 ^{+0.035} _{-0.037}	0.132 ^{+0.034} _{-0.033}

Table 2: Summary of the positron fraction results for the beta-fit, wavelets-fit and kernel with wavelets-fit. The errors are defined by the range between the 16th and the 84th percentiles in the R distributions.

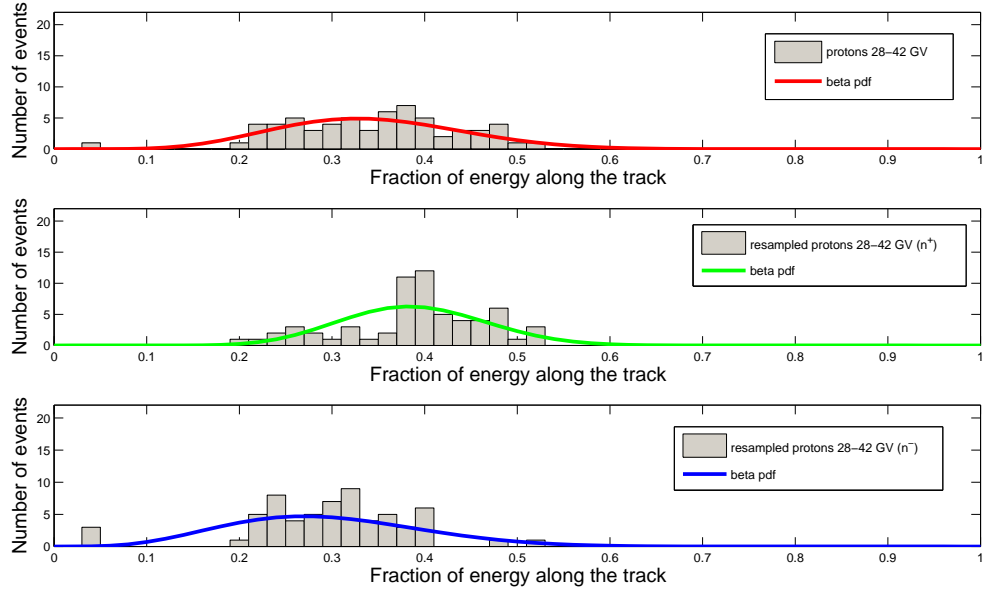


Figure 10: The distribution of positively charged particles selected as protons for the rigidity bin 28 - 42 GV and the same distribution when modified using the weighted bootstrap technique.

Fig. 10 shows protons for the rigidity bin 28 - 42 GV and the same distribution when modified using the weighted bootstrap technique. The range encompassing $R - R^+$ and $R + R^-$ is assumed as an estimate of the systematic uncertainty due the inaccuracies in the background selection. Tab. 3 reports the systematic uncertainties assessed for each rigidity bin.

Rigidity at spectrometer (GV)	Mean kinetic energy at top of payload beta-fit (GeV)	Extrapolated $\frac{\phi(e^+)}{\phi(e^-)+\phi(e^+)}$ at top of payload with beta-fit	Systematic uncertainties
1.5 – 1.8	1.65	0.0639 ^{+0.0017} _{-0.0017}	+0.0010 -0.0017
1.8 – 2.2	1.99	0.0591 ^{+0.0015} _{-0.0015}	+0.0011 -0.0018
2.2 – 2.7	2.44	0.0564 ^{+0.0015} _{-0.0015}	+0.0012 -0.0014
2.7 – 3.3	2.99	0.0549 ^{+0.0016} _{-0.0016}	+0.0012 -0.0013
3.3 – 4.1	3.67	0.0537 ^{+0.0017} _{-0.0017}	+0.0011 -0.0013
4.1 – 5.0	4.49	0.0545 ^{+0.0020} _{-0.0020}	+0.0018 -0.0014
5.0 – 6.1	5.68	0.0602 ^{+0.0024} _{-0.0024}	+0.0024 -0.0015
6.1 – 7.4	6.78	0.0522 ^{+0.0024} _{-0.0024}	+0.0024 -0.0016
7.4 – 9.1	8.27	0.0576 ^{+0.0028} _{-0.0028}	+0.0038 -0.0018
9.1 – 11.2	10.16	0.0570 ^{+0.0033} _{-0.0033}	+0.0028 -0.0019
11.2 – 15.0	13.11	0.0611 ^{+0.0032} _{-0.0033}	+0.0028 -0.0018
15.0 – 20.0	17.50	0.0630 ^{+0.0039} _{-0.0039}	+0.0033 -0.0020
20.0 – 28.0	23.99	0.0645 ^{+0.0052} _{-0.0052}	+0.0045 -0.0030
28.0 – 42.0	34.97	0.0733 ^{+0.0073} _{-0.0074}	+0.0057 -0.0044
42.0 – 65.0	53.43	0.090 ^{+0.012} _{-0.013}	+0.013 -0.008
65.0 – 100.0	82.39	0.106 ^{+0.028} _{-0.030}	+0.037 -0.044

Table 3: Summary of positron fraction results, obtained with the beta-fit, including statistical and systematic errors.

6. Experimental results and conclusions

Fig 11 shows the positron fraction R obtained through beta-fit with statistical and systematic errors summed in quadrature, compared with the PAMELA positron fraction previously reported [2]. The solid line shows a calculation by Moskalenko & Strong [40] for pure secondary production of positrons during the propagation of cosmic-rays in the galaxy. Proton-positron discrimination is provided by the imaging calorimeter, the capability to yield a trustworthy estimate of the positron and electron numbers in the cosmic radiation at energies between 1.5 GeV to 100 GeV has been clearly established. Compared to what is reported in [2]: a) new experimental data, b) the application of three novel background models and c) an estimate of the systematic uncertainties has been presented. The new experimental results are in agreement with what reported in [2] and confirm both solar modulation effects on cosmic-rays with low rigidities and an anomalous positron abundance above 10 GeV.

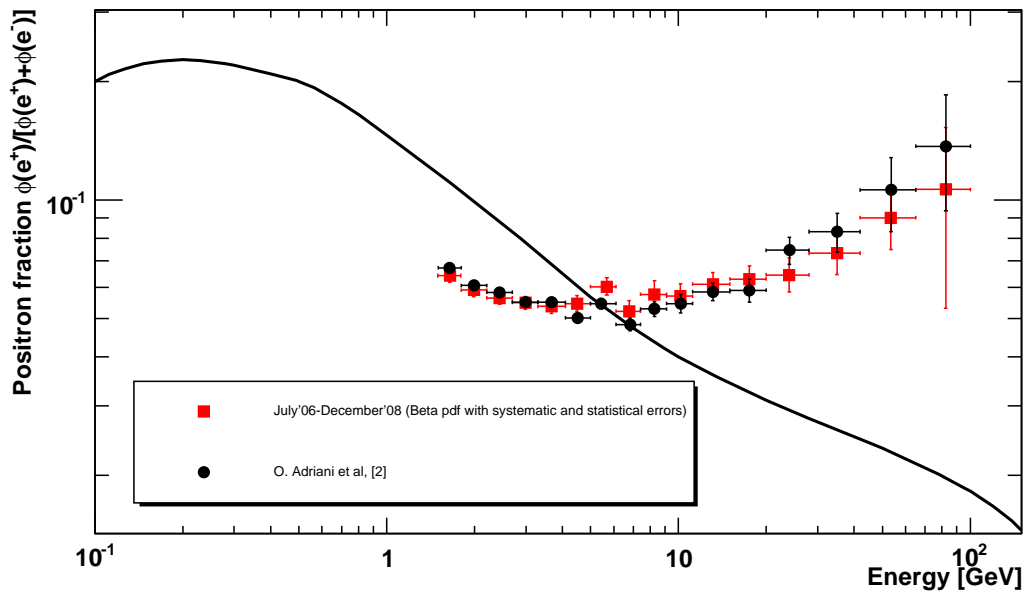


Figure 11: The positron fraction R obtained using a beta-fit with statistical and systematic errors summed in quadrature (red), compared with the positron fraction reported in [2] (black). The solid line shows a calculation by Moskalenko & Strong [40] for pure secondary production of positrons during the propagation of cosmic-rays in the galaxy.

- [1] J. Chang et al., Nature 456 (2008) 362.
- [2] O. Adriani et al., Nature 458 (2009) 607.
- [3] A. A. Abdo et al., Phys. Rev. Lett. 102 (2009) 181101.
- [4] F. Aharonian et al., Phys. Rev. Lett. 101 (2008) 261104.
- [5] S. Barwick et al., Phys. Rev. Lett. 75 (1995) 390.
- [6] R.L. Golden et al., Astrophys. J. 457 (1996) L103.
- [7] S. Barwick et al., Astrophys. J. Lett. 482 (1997) 191.
- [8] M. Boezio et al., Astrophys. J. 532 (2000) 653.
- [9] M. Aguilar et al., Phys. Rep. 366 (2002) 331.

- [10] J. J. Beatty et al., Phys. Rev. Lett. 93 (2004) 241102.
- [11] J. Alcaraz et al., Phys. Rept. 366 (2002) 331.
- [12] See, for example,
 - N. Arkani-Hamed et al., Phys. Rev. D 79 (2009) 015018;
 - V. Barger et al., Phys. Lett. B 672 (2009) 141;
 - A. Feldman, Z. Liu and P. Nath, Phys. Rev. D 79 (2009) 063509;
 - R. Harnik and G. D. Kribs, Phys. Rev. D 79 (2009) 095007.
- [13] M. Boezio et al., New J. Phys. 11 (2009) 105023.
- [14] O. Adriani et al., Phys. Rev. Lett. 102 (2009) 051101.
- [15] V.M. Abazov, Phys. Rev. D 78 (2008) 012005.
- [16] S. Ohm, C. van Eldik and K. Egberts, Astroparticle Physics 31 (2009) 383.
- [17] F. Aversa et al., Astroparticle Physics 5 (1996) 111.
- [18] R. Bellotti, M. Boezio and F. Volpe, Astroparticle Physics 22 (2005) 431.
- [19] P. Picozza et al., Astroparticle Physics 27 (2007) 296.
- [20] M. Boezio et al., Astroparticle Physics 26 (2006) 111.
- [21] R.L. Golden et al., Astrophys. J. 436 (1994) 769.
- [22] M. Boezio et al., Astrophys. J. 532 (2000) 653.
- [23] R. Bellotti et al., Astroparticle Physics 7 (1997) 219.
- [24] R. Brun et al., Detector Description and Simulation Tool, CERN program library (1994).
- [25] M.D. Hannam and W.J. Thompson, Nuclear Instrument and Methods in Physics Research A 431 (1999) 239.
- [26] B.S. Everitt and D.J. Hand, Finite Mixture distributions, (London, Chapman and Hall, 1981).

- [27] S. Baker, R.D.Cousins, Nuclear Instrument and Methods in Physics Research 221 (1984) 437.
- [28] V.K. Rohatgi, An Introduction to Probability Theory and Mathematical Statistics, (New York, Wiley, 1976).
- [29] S.G. Mallat, IEEE Transactions on Pattern Analysis and Machine Intelligence 11 (1989) 674.
- [30] F. Aristizabal and M. I. Glavinovicy, Biophysical Journal 85 (2003) 2170.
- [31] W. Hardle et al., Wavelets, Approximation and Statistical Applications. Lecture Notes in Statist. 129 (New York, Springer, 1998).
- [32] L. Wasserman, All of Nonparametric Statistics. Springer Texts in Statist. (New York, Springer, 2006).
- [33] L.Z. Fhang and R.L. Thews, Wavelets in Physics, (Singapore, World Scientific, 1998).
- [34] J.C. Nankervis, Computational Statistics and Data Analysis 49 (2005) 461.
- [35] C.Z. Money, R.D. Duval, BOOTSTRAPING: A Nonparametric Approach to Statistical Inference (Newbury Park, CA, Sage Univesity Paper, 1993).
- [36] K. Cranmer, Computer Physics Communications, 136 (2001) 198.
- [37] A. W. Bowman and A. Azzalini, Applied Smoothing Techniques for Data Analysis, (Oxford, Clarendon Press, 1997).
- [38] Song Xi Chen, Computational Statistics & Data Analysis 31 (1999) 131.
- [39] P. Barbe, P. Bertail, The Weighted Bootstrap, (New York, Springer, 1995).
- [40] I.V. Moskalenko, A.W. Strong, Astrophys. J. 493 (1998) 694.